Supporting Information

Single-Element Diffraction-Limited Fisheye Metalens

Mikhail Y. Shalaginov[†,*], *Sensong An*[‡], *Fan Yang*[†], *Peter Su*[†], *Dominika Lyzwa*[§], *Anuradha M. Agarwal*[†,‖], *Hualiang Zhang*[‡], *Juejun Hu*[†,‖,*], *and Tian Gu*[†,‖,*]

[†]Department of Materials Science & Engineering, Massachusetts Institute of Technology, Cambridge, MA 02139, USA

[‡]Department of Electrical & Computer Engineering, University of Massachusetts Lowell, Lowell, MA 01854, USA

[§]Department of Biological Engineering, Massachusetts Institute of Technology, Cambridge, MA 02139, USA

[‖]Materials Research Laboratory, Massachusetts Institute of Technology, Cambridge, MA 02139, USA

*Email: mys@mit.edu, hujuejun@mit.edu, gutian@mit.edu

1. Baseline metalens design using a standard hyperbolic phase profile

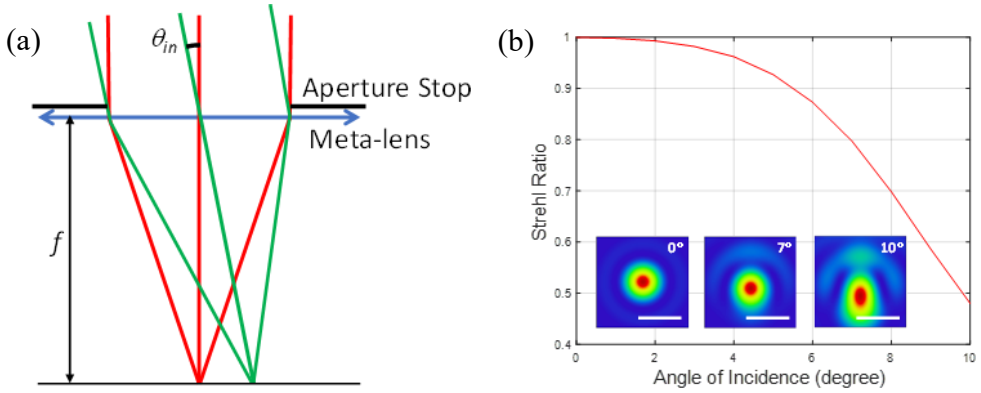

Fig. S1. (a) Schematic of a baseline metalens design based on the conventional hyperbolic phase profile; (b) simulation results of Strehl ratio vs. AOI; the scale bars represent 20 μm.

The prevailing method for designing a single-element metalens uses a hyperbolic phase profile to realize a spherical wavefront[1]:

$$\phi_0 = -\frac{2\pi}{\lambda}\left(\sqrt{f^2 + x^2 + y^2} - f\right) \tag{1}$$

where λ is the wavelength of incident light, x and y are the coordinates of meta-atoms, and f is the focal length of the metalens. While generating zero spherical aberration at the focal plane for a planar wavefront at normal incidence, such a phase profile is not optimized for obliquely incident beams. When a beam strikes the metasurface at an oblique incident angle (θ_x, θ_y), the desired phase profile becomes[2]:

$$\phi(\theta_x,\theta_y) = -\frac{2\pi}{\lambda}\left(\sqrt{f^2 + (x-x_0)^2 + (y-y_0)^2} - \sqrt{f^2 + x_0^2 + y_0^2} + \left(x\sin(\theta_x) + y\sin(\theta_y)\right)\right), \tag{2}$$

where $x_0 = f\tan(\theta_x)$, $y_0 = f\tan(\theta_y)$ are the coordinates of the focal spot.

Phase profile deviation due to different angles of incidence (AOIs) results in third-order (Seidel) aberrations such as coma, astigmatism, and field curvature, which limit the FOV. For the sake of comparison with our work, a baseline metalens operating at 5.2 μm wavelength was designed with

the same NA and input aperture size, as schematically illustrated in Figure S1a. As commonly configured, the baseline design uses a hyperbolic phase profile and position of the metasurface overlaps with that of the aperture stop. As shown in Figure S1b, such a design effectively suppresses spherical aberration with a Strehl ratio of unity at normal incidence. However, the Strehl ratio reduces below 0.8 as the AOI increases beyond ~ 7°, due to the exacerbated coma aberration.

2. Design of the WFOV metalens

The commercial optical design software OpticStudio® (Zemax, LLC) was used to obtain the initial phase profile of the metasurface under ideal conditions. The rotationally symmetric phase profiles are expressed in a polynomial form:

$$\phi(\rho) = \sum a_n \left(\frac{\rho}{R} \right)^{2n} , \tag{3}$$

where $\phi(\rho)$ is the desired phase response of specific meta-atoms with $\rho = \sqrt{x^2 + y^2}$, a_n are aspheric coefficients, and R is the normalization radius. The optimization starts with a standard hyperbolic phase profile consistent with the optical system specifications (i.e., focal length and *f*/#) over a small AOI range. Once the initial optimization cycle converges for the starting AOI range, the result is used as the input for the next optimization iteration cycle with an expanded AOI range. The process continues till the final result converges for a targeted AOI range (e.g., ± 90°). More specifically, numerical optimization using the Levenberg–Marquardt algorithm (also known as the damped least-squares method) is implemented to maximize the merit function (i.e. the FOM defined in Eq. 1 in the main text) in each optimization cycle. For the exemplary design, an initial angular interval of ΔAOI = 5° between neighboring beams is sufficient to sample the entire FOV continuously.

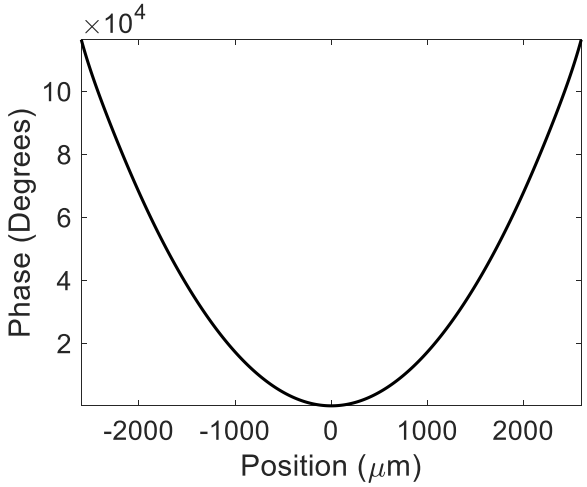

Fig. S2. The final phase profile of the WFOV metalens at $y = 0$. The 2-D phase map is rotationally symmetric.

Table S1. Phase profile design coefficients for mid-IR WFOV metalens

R (mm)	a_1	a_2	a_3	a_4	a_5	a_6	a_7
2.219e-3	-1492.12	232.31	-916.34	2179.49	-2829.43	1837.91	-467.25

Table S2. Phase profile design coefficients for NIR WFOV metalens

R (mm)	a_1	a_2	a_3	a_4	a_5	a_6	a_7	a_8	a_9	a_{10}
2.25e-3	-6708.07	63.55	-175.6	290.48	-264.77	106.33	16.11	-34.28	12.98	-1.69

The Kirchhoff diffraction integral is used to numerically calculate the Strehl ratio at each field angle as well as the FOM. Angular-dependent responses of each meta-atoms are also incorporated to generate angular-dependent phase/amplitude masks after spatial and phase discretization/mapping of the initial phase profile. In each optimization cycle, a FOM with equal weights for all AOIs over the range is initially used and maximized. Maximizing this equal-weight FOM can sometimes result in Strehl ratios less than 0.8 at some field angles. In this case, the optimization is repeated with adjusted weighting factors until the Strehl ratios are above 0.8 for all AOIs within the target range. The final phase profile (Figure S2) obtained with the procedure

achieves diffraction-limited focusing performance for continuously-varying incident angles up to ± 90°. The phase profile design coefficients are summarized in Table S1. Angular-dependent phase profiles (in the center 1-mm-diameter region) based on phase shifts of individual meta-atoms under different AOIs inside the substrate are shown in Figure S3.

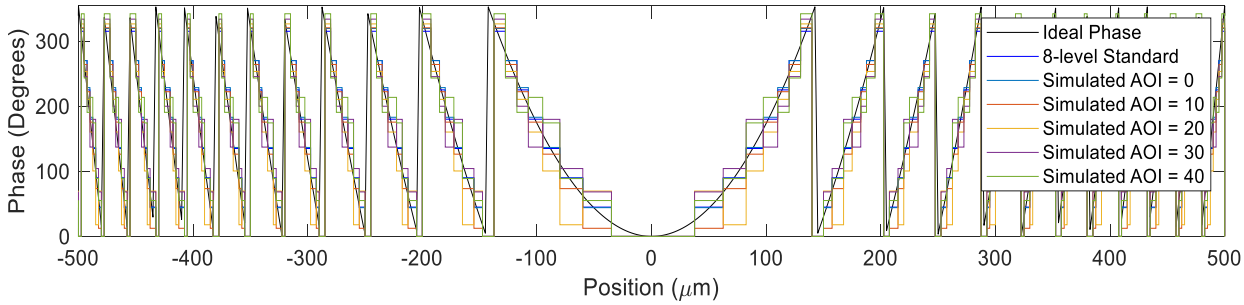

Fig. S3. Angular-dependent phase profiles of the center 1-mm-diameter region of the WFOV metasurface under different angles of incidence inside the substrate. At an incident angle of nearly 90° from air, the maximum angle of light propagation inside the substrate is 45.6°.

Table S3. Dimensions of meta-atoms used in the meta-optical devices.

Meta-atom number	1	2	3	4	5	6	7	8
L_x (L_{xd})	2.0 (0.6)	1.8 (0.6)	2.0 (0.7)	2	1.78	1.38	0.62	2
L_y (L_{yd})	1.7 (0.9)	1.9 (0.8)	1.6 (0.7)	0.78	0.7	0.66	0.52	1.26

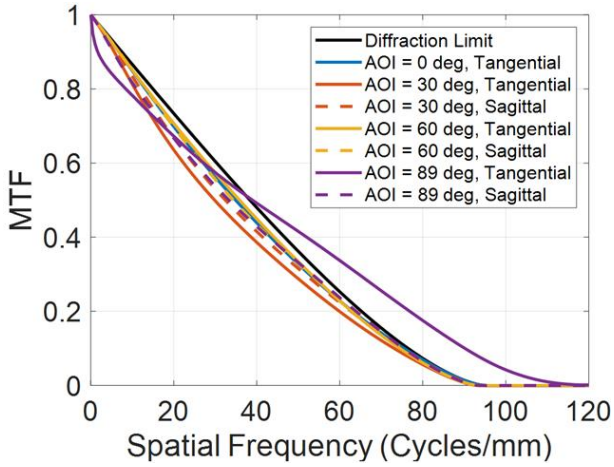

Fig. S4. Modulation transfer functions (MTF) of the simulated focal spots under different angles of incidence in the air.

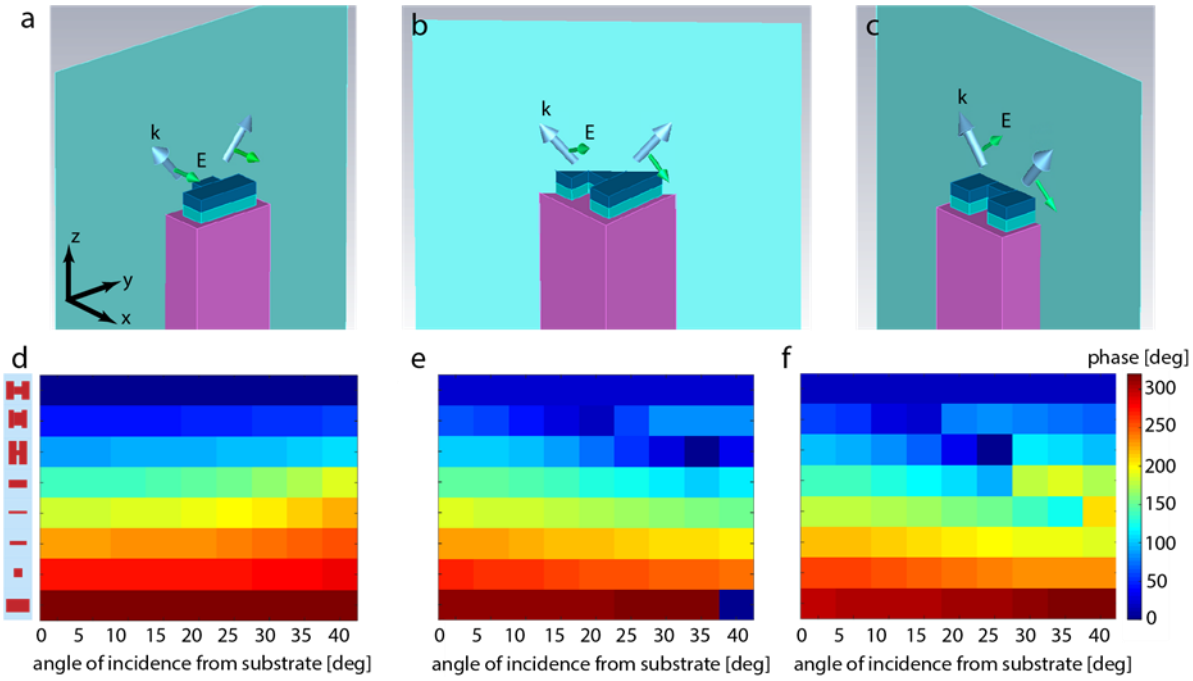

Fig. S5. Meta-atoms angular response for different linear polarization with oblique incidence at planes (a) *y*-*z*, (b) 45°- rotated between *y*-*z* and *x*-*z*, (c) *x*-*z* (TM-polarized). E-field *y*-component is equal to zero. At an incident angle of nearly 90° from air, the maximum angle of light propagation inside the substrate is 45.6°.

3. Metalens characterization.

For focal spot characterization, the metalens sample was mounted on a 3-axis translation stage and illuminated from the aperture side with a 5.2 μm collimated laser beam (Daylight Solutions, 21052-MHF-030-D00149). The laser was mounted on a mobile cart that can move along a custom-made circular rail (Figure 4a in the main text). Focal spot produced by a metalens was magnified with a custom-made microscope assembly (henceforth termed as magnifier), consisting of lens 1 (C037TME-E, Thorlabs Inc.) and lens 2 (LA8281-E, Thorlabs Inc.). Finally, magnified image of the focal spot was projected onto a liquid nitrogen cooled InSb FPA with 320 × 256 pixels (Santa Barbara Infrared, Inc.). Magnification of the microscope assembly was calibrated to be 120 ± 3

with a USAF resolution chart. The FPA and magnifier were fixed on a breadboard, therefore both of them can be controllably translated as a single piece perpendicular to the metalens optical axis. The incident beam angle was varied from 0° to 85° in 5° increments. Geometric constraints due to the circular rail and the mobile cart limit the maximum measurement angle to 85°. In the imaging setup (Figure 4j in the main text) the camera had to be rotated, since the compound lens (Asio lens 40494-AA1, f 25mm, Janos Tech) FOV is limited to 45°. Wide-angle imaging performance can alternatively be achieved by introducing a second large-FOV metalens to refocus the light incident at large angles into the camera image sensor focal plane. In the latter case, a rotating camera is not necessary. A pair of single-side polished silicon wafers were inserted into the optical path to reduce spatial coherence from the illuminating laser, thereby reducing speckles. The light scattered by the object is collected by the metalens and redirected to an FPA camera with attached compound lens.

The power focused by a metalens $P_{ms,foc}(\theta_i)$ can be expressed in terms of $P_0 cos(\theta_i)$ total incident power transmitted through the frontside aperture (1 mm circular aperture), metalens focusing efficiency $f(\theta_i)$, and Fresnel transmittance factor $T_p(\theta_i)$ accounting for reflection losses at the interface of air and CaF_2:

$$P_{ms,foc}(\theta_i) = T_P(\theta_i) f(\theta_i) P_0 \cos(\theta_i) . \quad (4)$$

The cosine factor appears when the same collimated laser beam incident obliquely on the sample, the power density penetrating through the aperture drops by a factor of $\cos(\theta_i)$ due to geometric projection.

In our experiments, we measured $\eta(\theta_i)$ – the ratio of focused to total transmitted power by metalens, $P_{ms,trans}(\theta_i)$ – power transmitted by metalens, and $P_{ref}(\theta_i)$ – power transmitted through a reference sample (a CaF_2 substrate with identical thickness and a 1 mm aperture but without the backside metasurface). By these definitions:

$$\eta(\theta_i) = P_{ms,\,foc}(\theta_i) / P_{ms,trans}(\theta_i) \ , \tag{5}$$

$$P_{ref}(\theta_i) = P_0 \cos(\theta_i) T_P^{\,2}(\theta_i) \ . \tag{6}$$

In Eq. 7, the $T_p(\theta_i)$ factor is squared because there are two CaF_2-air interfaces with identical transmittance. Finally, the value of focusing efficiency $f(\theta_i)$ is given by:

$$f(\theta_i) = \frac{P_{ms,\,foc}(\theta_i)}{P_0 \cdot T_P(\theta_i)\cos(\theta_i)} = \frac{\eta(\theta_i) P_{ms,trans}(\theta_i)}{P_0 T_P(\theta_i)\cos(\theta_i)} = \frac{\eta(\theta_i) P_{ms,trans}(\theta_i) T_P^{\,2}(0)}{P_{ref}(0) T_P(\theta_i)\cos(\theta_i)} \ . \tag{7}$$

$T_p(\theta_i)$ was calculated with a standard Fresnel formula and experimentally verified by measuring $P_{ref}(\theta_i)$ with a sensor featuring a large detection area of 18 × 18 mm^2 (S175C, Thorlabs Inc.). To quantify $\eta(\theta_i)$, we measured $P_{ms,foc}(\theta_i)$ the transmitted power incident upon a detector (S302, Thorlabs Inc.) integrated with a 200 μm diameter pin hole and $P_{ms,trans}(\theta_i)$ – transmitted power without a pinhole. We further used the InSb FPA camera to image the focal plane around the focal spot over a 200 μm diameter area to confirm that most of the focused light propagated through the pinhole is confined within the focal spot. The reason we could not directly read out the focused power from the camera is that the FPA does not give optical power readings and instead only specifies relative optical intensity in counts.

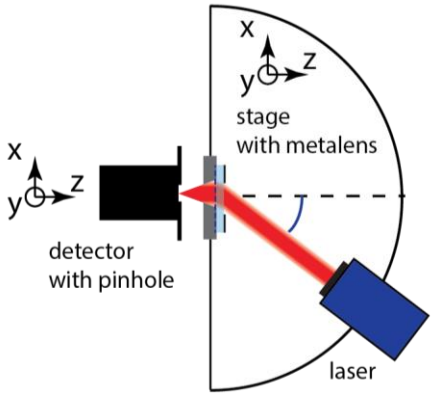

Fig. S6. Experimental layout for measuring metalens focusing efficiency.

4. NIR WFOV metalens design

The a-Si nano-posts have a uniform height of 750 nm, diameters ranging from 100 nm to 250 nm, and a fixed lattice constant of 450 nm. Full wave simulation results in Fig. S7a show that the design yields high transmittance for all eight meta-atoms, which together cover the full 2π phase space with a step of $\pi/4$ under normal incidence. The metasurface has an overall dimension of 6.4×6.4 mm^2, containing $14{,}222 \times 14{,}222$ meta-atoms on a 3.9-mm-thick sapphire substrate. The metasurface is designed to have a constant focal length of 2.5 mm and an image plane dimension of approximately 5×5 mm^2. A circular input aperture with a diameter of 1 mm is positioned on the front side of the substrate, corresponding to an effective NA of 0.2.

Figures S7b-d plot simulated transmittance and phase responses of the eight meta-atoms at different AOIs inside the substrate (corresponding to 0° to 90° AOIs in air). The results indicate that the phase responses of such high-index-contrast waveguide-type metatoms are almost independent of AOIs. The full-wave simulated meta-atom responses are incorporated in the metalens design presented in Fig. 5 in the main text. Figures S7b-d further suggest minimal polarization dependence of the meta-atom design. Polarization diversity of the NIR WFOV metalens design is validated by evaluating the focal spot intensity distribution, Strehl ratio, and focusing efficiency for both TE and TM polarizations at oblique incidence (Fig. S8). Differences in optical responses for the two polarizations are negligible for all AOIs over the full 180° FOV.

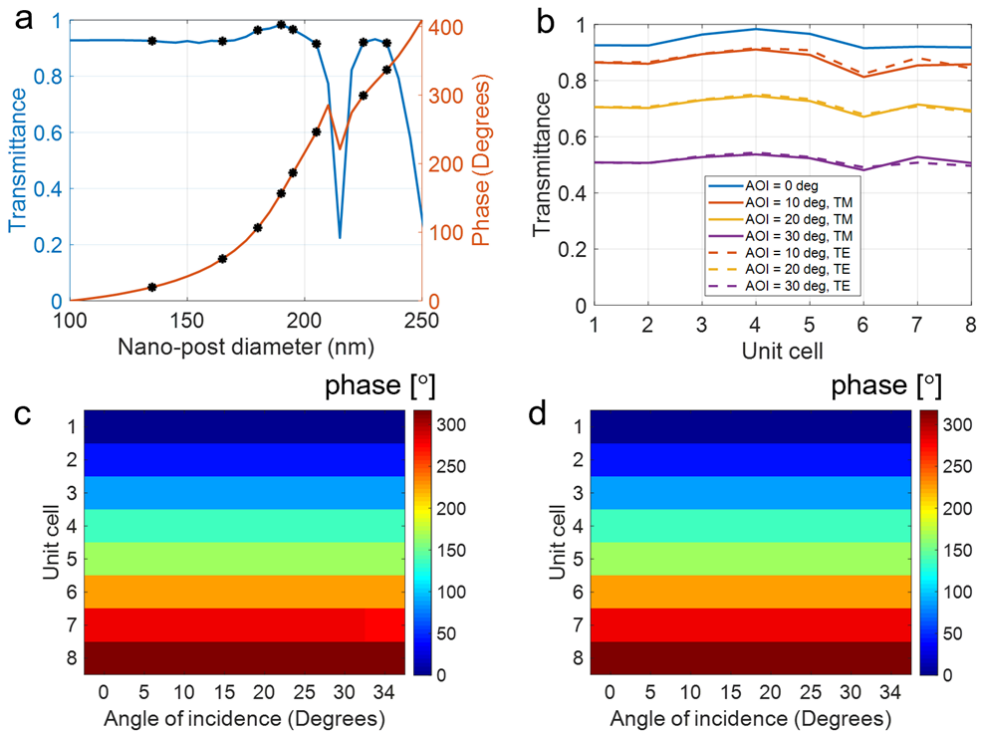

Fig. S7. (a) Simulated transmittance and phase shift of periodic a-Si nano-post arrays on an Al_2O_3 substrate under normal incidence. Selected meta-atoms used to construct the metalens are indicated by black markers. (b-d) Simulated optical responses at different AOIs (inside the substrate) of the eight meta-atoms: (b) transmittance and phase shifts of (c) TM and (d) TE polarized light.

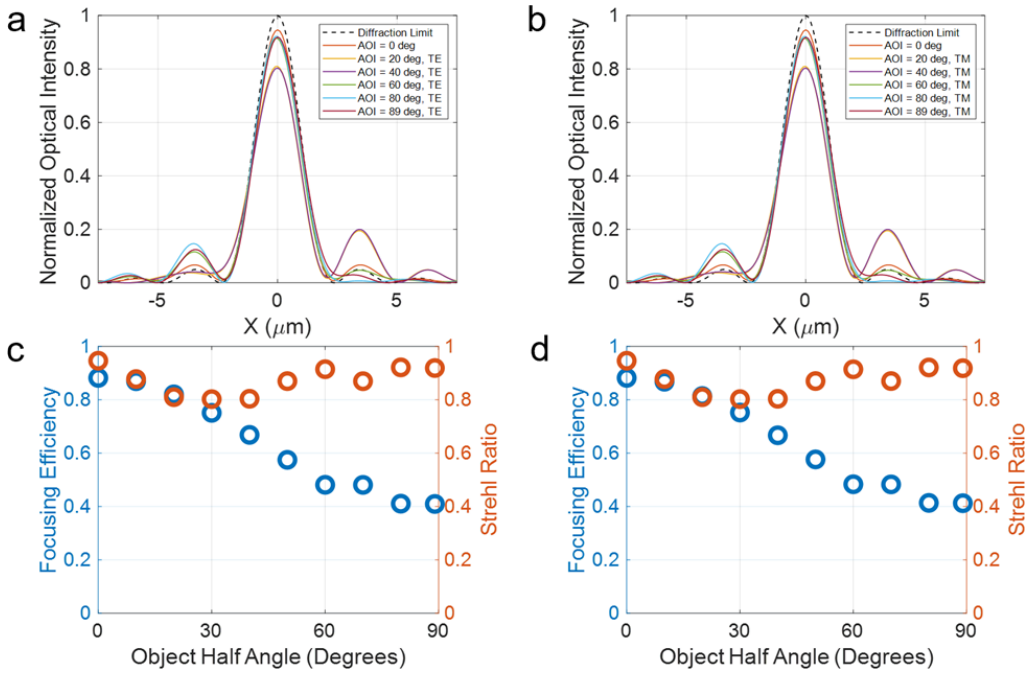

Fig. S8. Simulated metalens performance at different AOIs (in air): normalized optical intensity at the focal plane for (a) TE and (b) TM polarized light; Strehl ratios and focusing efficiencies for (c) TE and (d) TM polarized light.

5. NIR WFOV metalens image simulation

The imaging performance of the NIR WFOV metalens operating at a wavelength of 940 nm has been studied using OpticStudio's Image Simulation tool that evaluates diffraction, aberration and distortion effects, etc. of an imaging system. The object was mapped to the angular space (covering a horizontal FOV of 180° and a vertical FOV of 78°), equivalent to positioning the scene at an infinite distance away from the metalens. The source image contains 7,000 × 3,033 pixels, corresponding to a horizontal angular resolution of approximately 0.03°. This value is smaller than the diffraction-limited angular resolution of the WFOV metalens (~ 0.1°), and thus using the image as the scene offers adequate resolution to identify image blurring due to aberration or diffraction. During the simulation, the source image was convolved with a 2-D field-dependent point spread function (PSF) grid to generate the image at the image plane. Since our WFOV metalens readily

provides diffraction-limited PSFs across the entire 180° FOV, it enables a high-quality image with minimum aberrations.

6. An intuitive explanation of the WFOV performance

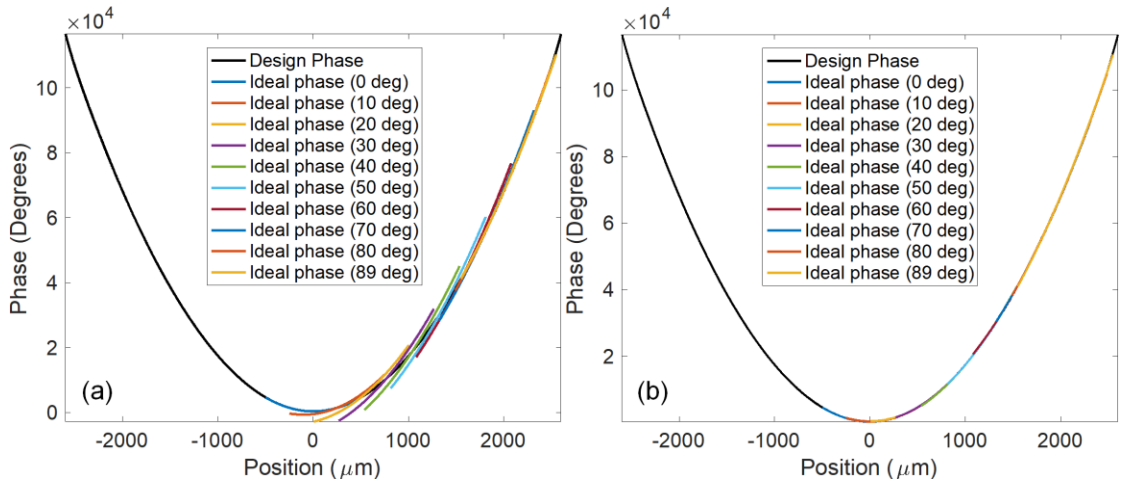

Fig. S9. (a) Overlay of the ideal phase profiles at different AOIs (measured in free space) with our optimized design phase (Fig. S2); (b) phase profiles similar to (a) except that each of the "ideal" phase profile was further "tilted" by adding another linear phase gradient to closely match the numerically optimized design phase.

To perfectly focus an obliquely incident beam perpendicularly onto a focal plane, the phase distribution within the aperture of a metalens must equal to the sum of a classical hyperbolic profile and a linear phase gradient, the latter of which accounts for the "tilted" wavefront of the obliquely incident beam. In our design, the beam is incident on a sub-region of the backside metasurface after being refracted by the substrate front surface through the aperture stop. We can then generate the ideal phase profiles over the sub-regions to perfectly focus light at different AOIs inside the substrate, which are translated from the AOIs in free space via the Snell's Law. These ideal phase profiles for different AOIs are plotted in Fig. S9 (a), along with the design phase of our WFOV metalens shown in Fig. S2. The figure suggests that the ideal phase profiles overlap with each

other and all closely align with the design phase, indicating the possibility of using one single phase profile (aka our design) to produce high-quality focusing at all the AOIs. The agreement between the design phase and the ideal phase profiles can be further improved if we are allowed to slightly "tilt" the latter, which is equivalent to adding a linear phase gradient to each of the ideal phase profiles. Fig. S9 (b) shows that the operation can lead to almost perfect agreement of the "tilted" phase profiles at all AOIs with the design phase. The maximum linear phase gradient we need to superimpose to yield Fig. S9 (b) corresponds to a 7° change in the beam incident angle. This result implies that the worst-case aberration resulting from our design across the entire FOV (caused by deviation of our design phase from the ideal phase profiles) is equivalent to the aberration induced by an obliquely incident beam with an AOI of 7° impinging upon a classical hyperbolic metalens with the same NA as our WFOV lens. This maximum aberration does not compromise diffraction-limited focusing quality according to Fig. S1b, which shows that for a hyperbolic metalens its Strehl ratio is ~ 0.8 at an AOI of 7°. This finding suggests that a single metasurface phase profile can indeed offer diffraction-limited focusing and imaging capabilities continuously across all AOIs.

From a design perspective, one can start with the isolated local ideal phase profiles at different AOIs and introduce minimally-tolerable phase deviations at each AOI to obtain a continuous phase profile with close approximations of the solution via optimization. In addition, the observation that the ideal phase profiles all significantly overlap with each other in Fig. S9a highlights the importance of simultaneously accounting for all AOIs in our optimization approach, and clearly distinguishes our design from spatially multiplexed metasurface architectures which only operate at discrete AOIs.

7. Imaging with the mid-IR WFOV metalens

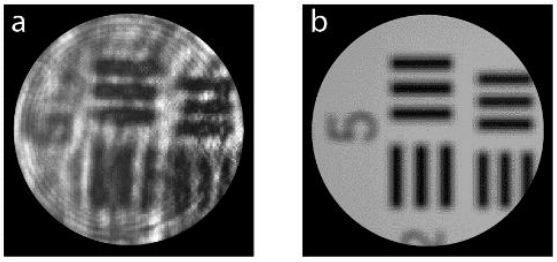

Fig. S10. The USAF resolution target (a) imaged by the WFOV metalens at normal incidence (same as Fig. 4k at 0° incidence); (b) imaged by a perfect aberration-free lens of the same numerical aperture, simulated using OpticStudio®. The fringes in the background of (a) are caused by laser speckles not completely removed by the Si wafer optical diffuser.

REFERENCES

(1) Aieta, F.; Genevet, P.; Kats, M. A.; Yu, N.; Blanchard, R.; Gaburro, Z.; Capasso, F. Aberration-Free Ultrathin Flat Lenses and Axicons at Telecom Wavelengths Based on Plasmonic Metasurfaces. *Nano Lett.* **2012**, *12* (9), 4932–4936.

(2) Kalvach, A.; Szabó, Z. Aberration-Free Flat Lens Design for a Wide Range of Incident Angles. *J. Opt. Soc. Am. B* **2016**, *33* (2), A66.